

Criticality of biochemical feedback

Amir Erez,^{1,*} Tommy A. Byrd,^{2,*} Robert M. Vogel,³ Grégoire Altan-Bonnet,¹ and Andrew Mugler^{2,†}

¹*Immunodynamics Group, Cancer and Inflammation Program, National Cancer Institute, National Institutes of Health, Bethesda, Maryland 20814, USA*

²*Department of Physics and Astronomy, Purdue University, West Lafayette, Indiana 47907, USA*

³*IBM T. J. Watson Research Center, Yorktown Heights, New York 10598, USA*

Biochemical feedback leads to dynamical transitions between cellular states, reminiscent of phase transitions in statistical physics. Yet it is unknown whether cells exhibit the scaling properties associated with phase transitions, and if they do, to which universality class or classes they belong. Here we show using a generic birth-death model that biochemical feedback near a bifurcation point exhibits the scaling exponents of the Ising universality class in the mean-field limit. The theory allows us to calculate an effective order parameter, temperature, external field, and heat capacity from T cell fluorescence data without fitting. Experiments agree with the scaling predictions, suggesting that this type of nonequilibrium criticality plays an important role in cell biology.

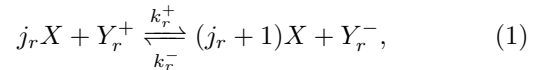
Certain biological behaviors are reminiscent of critical phenomena. A key example is biochemical feedback: positive feedback at the gene regulatory or signaling level can lead to a transition from one to two functional states, usually modeled as a bifurcation in a dynamical system or its stochastic analog [1–4]. This behavior is reminiscent of a phase transition in a physical system such as a fluid, magnet, or superconductor, where a disordered state transitions to one of two ordered states at a critical temperature [5]. The bifurcation point is the analog of the critical point. Yet critical points in physical systems satisfy very specific criteria, such as scaling laws, that place them in particular universality classes [5]. This raises a fundamental question: does biochemical feedback generically satisfy these scaling criteria near its transition point, and if so, to what universality class does it belong?

Recent experiments have shown that biological systems on all scales, from molecules [6], to cells [7–10], to populations [11, 12], exhibit signatures consistent with physical systems near a critical point. However, some of these signatures, particularly scaling laws, can arise even far from a critical point [13, 14] or can be alternatively explained without relying on criticality [15]. This highlights the need for a theoretical framework that can identify critical behavior [4, 16–18] and universality classes [19, 20] in biological systems from first principles, and generate falsifiable predictions for experiments.

Here we investigate the statistical physics of biochemical feedback near its dynamical transition point. We focus on a generic stochastic framework in which feedback is encapsulated in a birth-death process. We show that the system exhibits near its transition point the critical properties of the Ising universality class in the mean-field limit. Our theory gives quantitative predictions that we test, without fitting, using data on T cell signaling measured at the single-cell level [21]. The agreement of theory and experiment suggests that the critical behavior we uncover here plays an important role in immune response, and in cellular networks in general.

Consider a reaction network in a cell, where X is the

molecular species of interest, and A, B, C , etc. are the other species [Fig. 1(a)]. The other species form a chemical “bath” for X . The reactions of interest produce or degrade an X molecule, can involve the bath species, and in principle are reversible. We allow for nonlinear feedback on X , meaning that the production of an X molecule in a particular reaction might require a certain number of X molecules as reactants. This leads to a general set of R reactions of the form



where in each reaction $r \in \{1, 2, \dots, R\}$, the $j_r \in \{0, 1, 2, \dots\}$ are stoichiometric integers describing the nonlinearity, k_r^\pm are the forward (+) and backward (–) reaction rates, and Y_r^\pm represent the particular bath species involved as reactants (+) or products (–). A simple and well-studied special case of Eq. 1 is Schlögl’s second model [16, 22], in which X is either produced spontaneously from bath species A , or in a trimolecular reaction from two existing X molecules and bath species B (i.e., $R = 2$, $j_1 = 0$, $j_2 = 2$, $Y_1^+ = A$, $Y_2^+ = B$, and $Y_1^- = Y_2^- = \emptyset$). Early works argued that Schlögl’s second model belongs to the Ising universality class [23–25], although subsequent simulation studies have given conflicting results when spatial effects are included [19, 26, 27]. Eq. 1 is more general than Schlögl’s second model because it includes an arbitrary number R of birth-death reactions with arbitrary stoichiometry j_r . Because stoichiometry can influence universality class in biochemical models [20], it remains an open question to what, if any, universality class(es) Eq. 1 belongs.

Since every reaction in Eq. 1 involves the birth or death of one X molecule, the master equation for the probability of observing n such molecules is

$$\dot{p}_n = b_{n-1}p_{n-1} + d_{n+1}p_{n+1} - (b_n + d_n)p_n, \quad (2)$$

where $b_n = \sum_{r=1}^R J_{rn}^+$ and $d_n = \sum_{r=1}^R J_{rn}^-$ are the total birth and death propensities, and $J_{rn}^\pm = k_r^\pm n_r^+ n! / (n - j_r)!$

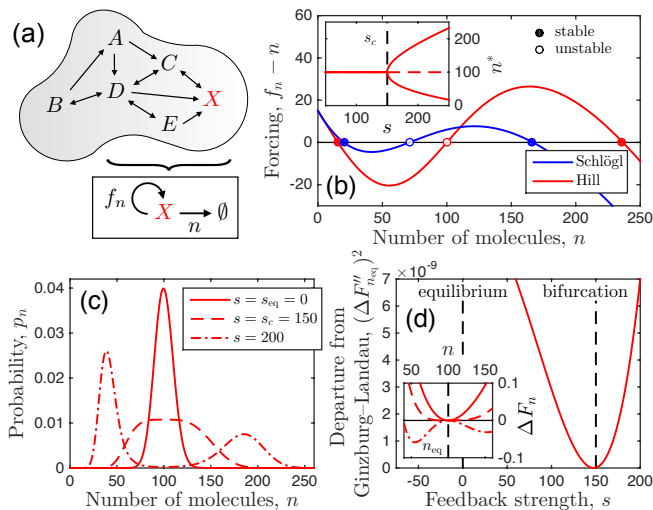


FIG. 1: (a) A generalized feedback function f_n (b) produces either one or two stable steady states, (c) corresponding to distributions that are one- or two-peaked, respectively, or flat at the bifurcation point. (d) The system at its bifurcation point behaves like a Ginzburg-Landau system at its critical point, as described in the text. Parameters are $H = 3$, $K = 126$, and $a = n_{\text{eq}} - s/3$ with $n_{\text{eq}} = 100$; in (b) $s = 255$. Legend in (c) also applies to inset of (d).

and $J_{r_n}^- = k_r^- n_r^- n! / (n - j_r - 1)!$ are the forward and backward propensities of each reaction pair. Here n_r^\pm are the numbers of molecules of the bath species involved in reaction r , and the factorials account for the number of ways that X molecules can meet in a reaction. We assume that the molecules are well-mixed and that the reaction rates and the numbers of bath molecules are constants in the model. The steady state of Eq. 2 is

$$p_n = p_0 \prod_{j=1}^n \frac{b_{j-1}}{d_j} = \frac{p_0}{n!} \prod_{j=1}^n f_j, \quad (3)$$

where $p_0^{-1} = \sum_{n=0}^{\infty} (1/n!) \prod_{j=1}^n f_j$ is set by normalization. In the second step of Eq. 3 we recognize that p_n depends only on the ratio of birth and death propensities, and therefore we define an effective birth propensity $f_n \equiv n b_{n-1} / d_n$ corresponding to spontaneous death with propensity n [Fig. 1(a)].

The function f_n encodes the feedback in our model. For Schlögl's second model, the feedback function is

$$f_n = \frac{aK^2 + s(n-1)(n-2)}{(n-1)(n-2) + K^2} \quad (\text{Schlögl}), \quad (4)$$

where we have introduced the dimensionless quantities $a \equiv k_1^+ n_A / k_1^-$, $s \equiv k_2^+ n_B / k_2^-$, and $K^2 \equiv k_1^- / k_2^-$. In general, f_n is an arbitrary, nonlinear function governed by the reaction network. As a generic example we also consider the Hill function with coefficient H ,

$$f_n = a + s \frac{n^H}{n^H + K^H} \quad (\text{Hill}). \quad (5)$$

The quantity $f_n - n$ determines the dynamic stability. It is plotted for Eqs. 4 and 5 in Fig. 1(b). In both cases, we see three steady states n^* where $f_{n^*} - n^* = 0$, two of which are stable (negative slope). Depending on the parameters, there can be either one or two stable states. For example, when a and s are covaried to the Hill function, a transition from a monostable to a bistable regime occurs at the bifurcation point s_c [Fig. 1(b) inset]. Stochastically, these regimes correspond to unimodal and bimodal distributions p_n , respectively, while the bifurcation point corresponds to a distribution that is flat on top [Fig. 1(c)].

Thermodynamic equilibrium occurs when the system obeys detailed balance, meaning that the forward flux balances the backward flux for every reaction r , i.e. $J_{r,n-1}^+ p_{n-1} = J_{r,n}^- p_n$. In this case, the distribution $p_n^{\text{eq}} = e^{-n_{\text{eq}}} (n_{\text{eq}})^n / n!$ is Poissonian [28–30], corresponding from Eq. 3 to a constant feedback function $f_n = n_{\text{eq}}$ [see Fig. 1(c) with $s = s_{\text{eq}} = 0$]. This is expected, since in equilibrium the system obeys the grand canonical distribution, which when summed over energies is Poissonian [31]. However, the bifurcation point occurs out of equilibrium.

Out of equilibrium, it is tempting to follow time-dependent Ginzburg-Landau theory [32, 33] and interpret Eq. 3 in the language of the canonical distribution: $p_n \propto e^{-U_n}$, where U_n is a dimensionless “energy,” and $F_n = -\partial_n U_n = \partial_n \log p_n$ is the associated dimensionless “force.” At the same time, Fig. 1(b) independently suggests a force that is proportional to $f_n - n$, namely $\tilde{F}_n = -\partial_n \tilde{U}_n = (f_n - n) / n_{\text{eq}}$ [34]. Because we cannot assume that p_n obeys the canonical distribution out of equilibrium (even in equilibrium it is *grand* canonical), F_n and \tilde{F}_n are, in general, different [35]. However, we see in the inset of Fig. 1(d) that at the bifurcation point s_c (dashed), the difference $\Delta F_n = F_n - \tilde{F}_n$ becomes small, especially around n_{eq} . We quantify this observation by computing the squared curvature $(\Delta F_{n_{\text{eq}}}'')^2$, and indeed, in Fig. 1(d) we see that this measure vanishes at the bifurcation point. This behavior can be understood from Eq. 3. For large n we have $F_n = \partial_n \log p_n \approx \log f_n - \log n = \log[1 + (f_n - n)/n]$. At the bifurcation point, f_n is tangent to n at n_{eq} . This creates the largest range of n over which $f_n - n$ is small, which permits the expansion of F_n around n_{eq} as $F_n \approx (f_n - n) / n_{\text{eq}} = \tilde{F}_n$. Thus, at the bifurcation point the two forces agree. This suggests that our system at its nonequilibrium bifurcation point behaves like an Ginzburg-Landau system at its critical point [24]. We thus return to our central question: does our model exhibit critical scaling, as a Ginzburg-Landau system does, and if so, to what universality class does it belong?

To address this question, we investigate the scaling properties of p_n . The extrema satisfy $0 = \partial_n p_n$, or equivalently $0 = \partial_n \log p_n = F_n \approx \tilde{F}_n \propto f_n - n$, where we have seen that the approximation is valid near

the bifurcation point. We expand f_n to third order around a point n_c that we are free to choose. Choosing n_c such that $f''_{n_c} = 0$ as in the Ginzburg–Landau critical point, the condition for extrema n_* becomes $0 = f_{n_c} + f'_{n_c}(n_* - n_c) + f'''_{n_c}(n_* - n_c)^3/3! - n_*$. We then define the parameters

$$m \equiv \frac{n_* - n_c}{n_c}, \quad h \equiv \frac{2(f_{n_c} - n_c)}{-f'''_{n_c} n_c^3}, \quad \theta \equiv \frac{2(1 - f'_{n_c})}{-f'''_{n_c} n_c^2}, \quad (6)$$

in terms of which the condition becomes

$$0 = h - \theta m - \frac{1}{3} m^3. \quad (7)$$

Eq. 7 is equivalent to the expansion of the Ising mean field equation $m = \tanh[(m + h)/(1 + \theta)]$ for small magnetization m , where $\theta = (T - T_c)/T_c$ is the reduced temperature, and h is the magnetic field times the magnetic moment over the product of the coupling energy and coordination number [33]. Therefore in our system we interpret m as the order parameter, θ as a reduced “temperature,” and h as a dimensionless “field.” θ refers to an effective temperature, distinct from the actual temperature of the system when it is in equilibrium. Positive (negative) θ drives the system to the unimodal (bimodal) state, while positive (negative) h biases the system to high (low) molecule numbers. Indeed, the covariation of a and s in Fig. 1 is determined by the condition $h = 0$ (see Table I [36]). The fact that the high-molecule number peak in Fig. 1(c) is fatter and lower than the low-molecule number peak is due to the scaling of fluctuations with molecule number in a birth-death process.

Eq. 7 implies that our system has the same scaling exponents β , γ , and δ as the Ising universality class in the mean-field limit [33]. The emergence of mean-field exponents is expected given that our model is well-mixed, meaning that each molecule interacts with every other molecule. Specifically, when $h = 0$, Eq. 7 becomes $0 = m(\theta + m^2/3)$; thus the maxima of p_n satisfy $m = 0$ or $m = \pm(-3\theta)^\beta$ when $\theta > 0$ or $\theta < 0$, respectively, with $\beta = 1/2$. Defining the dimensionless susceptibility $\chi \equiv (\partial_h m)_{h=0}$ and differentiating Eq. 7 gives $\chi = \theta^{-\gamma}$ or $\chi = (-2\theta)^{-\gamma}$ for $\theta > 0$ or $\theta < 0$, respectively, with $\gamma = 1$. Finally, when $\theta = 0$, Eq. 7 becomes $m = (3h)^{1/\delta}$, with $\delta = 3$. These scaling results are tested for the Schlögl and Hill models in Fig. 2(a)–(c), and we see excellent agreement.

The exponent α concerns the heat capacity, $C|_{h=0} \sim |\theta|^{-\alpha}$. The equilibrium definition $C = T\partial_T S$ generalizes to nonequilibrium when one uses the Shannon entropy $S = -k_B \sum_n p_n \log p_n$ [37]. In our case $T = (1 + \theta)T_c$ is the effective temperature, such that $C = (1 + \theta)\partial_\theta S$, or

$$\frac{C}{k_B} = -(1 + \theta) \sum_{n=0}^{\infty} p_n (1 + \log p_n) \left(\psi_n - \sum_{j=0}^{\infty} p_j \psi_j \right), \quad (8)$$

where $\psi_n \equiv (1/2)f'''_{n_c} n_c^2 \sum_{j=1}^n (j - n_c)/f_j$. Eq. 8 follows from performing the θ derivative using the expression in

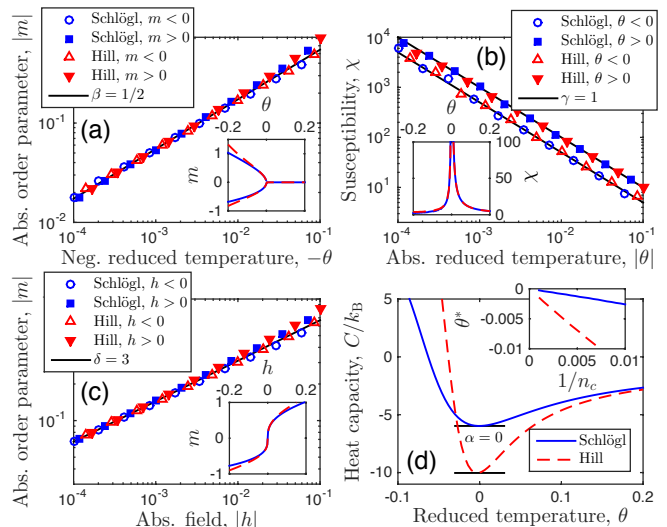


FIG. 2: Critical exponents α , β , γ , and δ of biochemical feedback near its nonequilibrium bifurcation point agree with those of the Ising universality class in the mean-field limit. Parameters are $H = 3$; $n_c = 500$; $h = 0$ in (a), (b), and (d); $\theta = 0$ in (c); and K , a , and s calculated from n_c , θ , and h according to Eq. 6 (see Table I [36]). (b) uses $m < 0$ maximum for $\theta < 0$; results are similar for $m > 0$. Legend in (d) also applies to all insets.

Eq. 3, the expansion above Eq. 6, and the definition of θ (Eq. 6). Testing α is more stringent than testing β , γ , and δ , since C is a function not just of the extrema of p_n , but of the entire distribution. We see in Fig. 2(d) that when $h = 0$, C exhibits a minimum at θ^* , and the inset shows that θ^* vanishes as the system size increases, $n_c \rightarrow \infty$. This implies $C|_{h=0} \sim |\theta|^0$ to sub-quadratic order in θ , or $\alpha = 0$, again consistent with the Ising universality class in the mean-field limit. Interestingly, whereas C is discontinuous in the mean-field Ising model [33] and constant in the van der Waals model of a fluid [5], it is minimized here; nevertheless, in all cases $\alpha = 0$. C is negative near $\theta = 0$ [Fig. 2(d)]; negative heat capacity is a well-known feature of nonequilibrium steady states [38–40].

We test our theory against experiments using measurements in T cells of doubly phosphorylated ERK (ppERK), which is subject to feedback via the MAP-kinase signaling cascade [21]. Six chemotherapy drugs inhibit key enzymes in the cascade (MEK, SRC), leading to either bimodal (low dose) or unimodal (high dose) distributions of ppERK abundance, measured as fluorescence intensity I by flow cytometry [Fig. 3(a)] [21, 36]. We anticipate that applying the drugs is similar to tuning the temperature and/or field in the theory. We derive these parameters from the intensity distributions using the following procedure (see Supplementary Information for full details [36]). First, we set $n = I/I_1$, where the

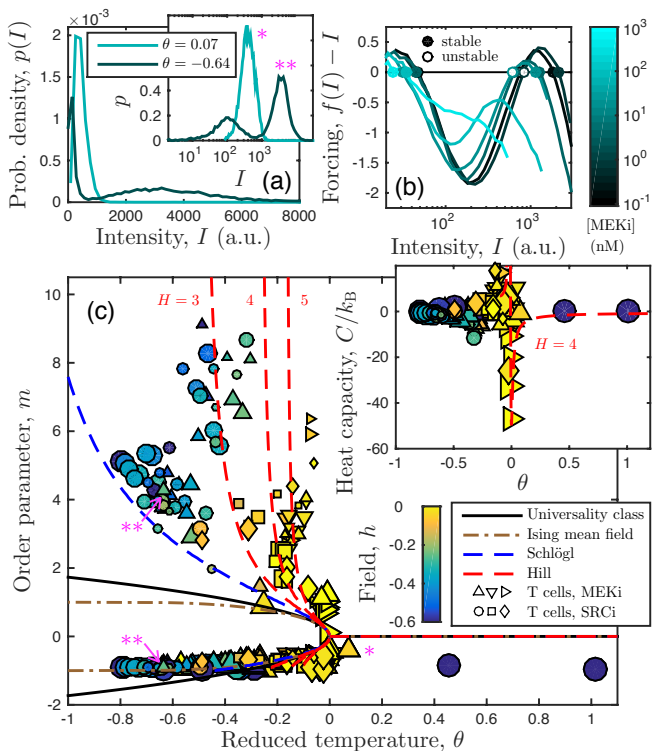


FIG. 3: Comparing theory and experiment. (a) Experimental distributions of T cell ppERK fluorescence intensity are bimodal (unimodal) under low (high) doses of inhibitor. Legend shows θ calculated by Eq. 6. (b) Feedback functions extracted from distributions yield criticality parameters (Eq. 6, 8). (c) Order parameter and heat capacity data agree with theory, particularly for $h \approx 0$ (yellow data) where theory is shown. See Table S2 [36] for drugs (shape) and doses (size). Magenta asterisks indicate data points in (c) corresponding to distributions in (a). Parameters are $W/L = 25/100$ in (b) and (c), $I_1 = 0.1$ in inset of (c), and $h = 0$ and $n_c = 7,300$ (mean experimental value) for Schlögl and Hill models.

intensity of one molecule I_1 is determined as described shortly. Next, we invert Eq. 3 to obtain the effective feedback function $f_n = np_n/p_{n-1}$ from the distribution [41]. Because the distributions are long-tailed, we calculate f from $\log I$ for numerical stability [Fig. 3(a) inset]. Additionally we smooth f and its derivatives using a Savitzky–Golay filter [42] with window size W . Finally, we calculate m , θ , and h from f (Eq. 6), and C from f and p_n (Eq. 8). This procedure requires the adjustable parameter W/L , where L is the number of $\log I$ bins, but no fitting. Results are robust to W/L [36].

Several expected results validate the analysis. First, distributions with $\theta > 0$ are unimodal (high dose), while bimodal distributions (low dose) have $\theta < 0$ [Fig. 3(a)]. Second, as expected from Fig. 1(b), we see in Fig. 3(b) that the quantity $f(I) - I$ has one stable state when the distribution is unimodal (light cyan), and two stable states when the distribution is bimodal (dark cyan).

Third, as found previously [21], the location of the high stable state changes with MEK inhibitor but not SRC inhibitor [36].

Fig. 3(c) shows the $h = 0$ predictions from the theory (blue and red), the mean-field Ising model (brown), and the universality class to which they belong (Eq. 7; black). All coincide at the critical point ($m = \theta = 0$). The lower branches ($m < 0$) of the biochemical and Ising models obey $m \geq -1$ because the number of molecules and up-spins is nonnegative, respectively (Eq. 6). Whereas the upper branch ($m > 0$) of the Ising model obeys $m \leq 1$ since the total number of spins is fixed, those of the biochemical models rise steeply since the molecule number is unbounded from above. The data points in Fig. 3(c) show m vs. θ for all drugs (shape) and doses (size), colored according to h . Most data have $\theta \lesssim 0$, since doses are sufficiently low to maintain a non-negligible high state; and $h \lesssim 0$, due to the long tails and the possible impact of autofluorescence [36]. We see that the data agree with the predictions in several important ways: (i) no data exist between the branches; (ii) data near $m = \theta = 0$ have $h \approx 0$ (yellow); (iii) the data closely follow the lower branch and obey $m \geq -1$; and (iv) the data exhibit the steep rise of the upper branch in the biochemical models, particularly the Hill function with $H \sim 4$. Fig. S3 [36] further demonstrates consistency of the data with the prediction $\beta = 1/2$ and with the known β - and δ -dependent scaling form of m , θ , and h [43].

The inset of Fig. 3(c) shows the $h = 0$ prediction for C with $H = 4$ (red), along with the data. We see that the two agree, particularly for data with $h \approx 0$ (yellow) as expected. A key feature for criticality, a global minimum in C at $\theta = h = 0$, is exhibited by the data and is robust to the choice of I_1 over four orders of magnitude [36]. Importantly, the depth of the minimum agrees with that of the theory only for $I_1 \sim 0.1$ as in the inset, corresponding to $n_* \approx 35,000$ molecules in the high mode without inhibition [36], in agreement with previous measurements on these cells [44, 45]. Thus the heat capacity allows estimation of absolute molecule number from fluorescence data. The agreement between theory and data in Fig. 3(c) is especially striking given that the theory is derived assuming a birth-death process, whereas the experimental distributions show long tails suggestive of more complex mechanisms such as bursting [46, 47] or cell-to-cell variability [48]. This suggests that the critical behavior we identify may describe biochemical feedback beyond even the generic model we consider.

We have shown that a generic model of biochemical feedback near its dynamic transition point exhibits the scaling properties of the Ising universality class in the mean-field limit. By discovering the effective order parameter, temperature, external field, and heat capacity of the system, we have quantitatively translated both the model and T cell fluorescence data into the language of statistical physics. Doing so has revealed agreement be-

tween the data and falsifiable predictions of the theory, with no fitting, suggesting that this class of nonequilibrium critical behavior plays an important role in cell biology. It will be interesting to see whether our framework allows one to further classify diverse biological systems under one or several universality classes.

This work was supported by Human Frontier Science Program grant LT000123/2014 (A. E.), Simons Foundation grant 376198 (T. A. B. and A. M.), and, in part, by the Intramural Research Program of the NIH, Center for Cancer Research, NCI.

* These authors contributed equally.

† Electronic address: amugler@purdue.edu

- [1] J. Hornos, D. Schultz, G. Innocentini, J. Wang, A. Walczak, J. Onuchic, and P. Wolynes, *Physical Review E* **72**, 051907 (2005).
- [2] G. Tkačik, A. M. Walczak, and W. Bialek, *Physical Review E* **85**, 041903 (2012).
- [3] J. Das, M. Ho, J. Zikherman, C. Govern, M. Yang, A. Weiss, A. K. Chakraborty, and J. P. Roose, *Cell* **136**, 337 (2009).
- [4] S. J. Ridden, H. H. Chang, K. C. Zygalkakis, and B. D. MacArthur, *Physical review letters* **115**, 208103 (2015).
- [5] N. Goldenfeld, *Lectures on phase transitions and the renormalization group*, vol. 5 (Addison-Wesley Reading, MA, 1992).
- [6] T. Mora, A. M. Walczak, W. Bialek, and C. G. Callan, *Proceedings of the National Academy of Sciences* **107**, 5405 (2010).
- [7] D. B. Kastner, S. A. Baccus, and T. O. Sharpee, *Proceedings of the National Academy of Sciences* **112**, 2533 (2015).
- [8] D. Krotov, J. O. Dubuis, T. Gregor, and W. Bialek, *Proceedings of the National Academy of Sciences* **111**, 3683 (2014).
- [9] G. De Palo, D. Yi, and R. Endres, *bioRxiv* p. 086538 (2016).
- [10] X. Chen, X. Dong, A. Be'er, H. L. Swinney, and H. Zhang, *Physical Review Letters* **108**, 148101 (2012).
- [11] W. Bialek, A. Cavagna, I. Giardina, T. Mora, O. Pohl, E. Silvestri, M. Viale, and A. M. Walczak, *Proceedings of the National Academy of Sciences* **111**, 7212 (2014).
- [12] A. Attanasi, A. Cavagna, L. Del Castello, I. Giardina, S. Melillo, L. Parisi, O. Pohl, B. Rossaro, E. Shen, E. Silvestri, et al., *Physical Review Letters* **113**, 238102 (2014).
- [13] D. Belitz, T. Kirkpatrick, and T. Vojta, *Reviews of modern physics* **77**, 579 (2005).
- [14] D. A. Kessler and H. Levine, *arXiv preprint arXiv:1508.02414* (2015).
- [15] D. J. Schwab, I. Nemenman, and P. Mehta, *Physical Review Letters* **113**, 068102 (2014).
- [16] F. Schlögl, *Zeitschrift für Physik* **253**, 147 (1972).
- [17] M. Pal, S. Ghosh, and I. Bose, *Physical biology* **12**, 016001 (2014).
- [18] H. Qian, P. Ao, Y. Tu, and J. Wang, *Chemical Physics Letters* **665**, 153 (2016).
- [19] P. Grassberger, *Zeitschrift für Physik B Condensed Matter* **47**, 365 (1982).
- [20] T. Ohtsuki and T. Keyes, *Physical Review A* **35**, 2697 (1987).
- [21] R. M. Vogel, A. Erez, and G. Altan-Bonnet, *Nature Communications* **7**, 12428 (2016).
- [22] This is not to be confused with the first biochemical model that Schlögl introduced in the same paper, which is known to be in the directed percolation universality class [19, 49].
- [23] G. Dewel, D. Walgraef, and P. Borckmans, *Zeitschrift für Physik B Condensed Matter* **28**, 235 (1977).
- [24] G. Nicolis and M. Malek-Mansour, *Journal of Statistical Physics* **22**, 495 (1980).
- [25] M. Brachet and E. Tirapegui, *Physics Letters A* **81**, 211 (1981).
- [26] S. Prakash and G. Nicolis, *Journal of Statistical Physics* **86**, 1289 (1997).
- [27] D.-J. Liu, X. Guo, and J. W. Evans, *Physical Review Letters* **98**, 050601 (2007).
- [28] M. Vellela and H. Qian, *Journal of the Royal Society Interface* **6**, 925 (2009).
- [29] C. W. Gardiner et al., *Handbook of stochastic methods*, vol. 3 (Springer Berlin, 1985).
- [30] Inserting the expressions for J_{rn}^{\pm} (see Eq. 2), the detailed-balance condition becomes $p_n/p_{n-1} = J_{r,n-1}^+/J_{rn}^- = k_r^+ n_r^+ / (k_r^- n_r^- n)$. Since p_n/p_{n-1} is not r -dependent, $k_r^+ n_r^+ / (k_r^- n_r^-)$ is constant for all r , which provides the constraints on the reaction rates that prevent flux cycles from forming in the state space. Calling this constant n_{eq} , we have $p_n/p_{n-1} = n_{eq}/n$, which is solved by the Poisson distribution.
- [31] C. Kittel and H. Kroemer, *Thermal physics* (1998).
- [32] P. C. Hohenberg and B. I. Halperin, *Reviews of Modern Physics* **49**, 435 (1977).
- [33] P. Kopietz, L. Bartosch, and F. Schütz, *Introduction to the functional renormalization group*, vol. 798 (Springer, 2010).
- [34] The proportionality factor $1/n_{eq}$ is set by the fact that when $f_n = n_{eq}$ at equilibrium, $\tilde{p}_n \propto e^{-\tilde{U}_n}$ should be the Gaussian approximation to the Poisson p_n .
- [35] Indeed, van Kampen emphasizes that only for diffusion-like processes, where the scale of fluctuations is set by a constant temperature, are U_n and \tilde{U}_n (and thus F_n and \tilde{F}_n) the same; for birth-death processes like the one we study here, where fluctuations scale with molecule number, they are different [50].
- [36] See Supplementary Information.
- [37] D. Mandal, *Physical Review E* **88**, 062135 (2013).
- [38] R. Zia, E. Praestgaard, and O. Mouritsen, *American Journal of Physics* **70**, 384 (2002).
- [39] E. Boksenbojm, C. Maes, K. Netočný, and J. Pešek, *EPL (Europhysics Letters)* **96**, 40001 (2011).
- [40] J. Bisquert, *American Journal of Physics* **73**, 735 (2005).
- [41] A. M. Walczak, A. Mugler, and C. H. Wiggins, *Proceedings of the National Academy of Sciences* **106**, 6529 (2009).
- [42] A. Savitzky and M. J. Golay, *Analytical Chemistry* **36**, 1627 (1964).
- [43] D. Gaunt and C. Domb, *Journal of Physics C: Solid State Physics* **3**, 1442 (1970).
- [44] G. Altan-Bonnet and R. N. Germain, *PLoS Biology* **3**, e356 (2005).
- [45] J. L. Hukelmann, K. E. Anderson, L. V. Sinclair, K. M.

	Schlögl	Hill
Feedback function	$f_n = \frac{aK^2 + s(n-1)(n-2)}{(n-1)(n-2) + K^2}$	$f_n = a + s \frac{n^H}{n^H + K^H}$
Critical value (at which $f''_{n_c} = 0$)	$n_c = \frac{3}{2} + \frac{1}{6} \sqrt{3(4K^2 - 1)}$	$n_c = K \left(\frac{H-1}{H+1} \right)^{1/H}$
Expansion coefficients	$f_{n_c} = \frac{(3a+s)K^2 - s}{4K^2 - 1}$ $f'_{n_c} = (s - a)K^2 \left(\frac{3}{4K^2 - 1} \right)^{3/2}$ $f'''_{n_c} = -6(s - a)K^2 \left(\frac{3}{4K^2 - 1} \right)^{5/2}$	$f_{n_c} = a + \left(\frac{H-1}{2H} \right) s$ $f'_{n_c} = \frac{(H^2 - 1)s}{4Hn_c}$ $f'''_{n_c} = -\frac{(H^2 - 1)^2 s}{8Hn_c^3}$
Inversion (where $x \equiv 2n_c - 3$)	$K^2 = \frac{1}{4}(3x^2 + 1)$ $s = \frac{3n_c^3(\theta+h) + n_c x^2 + x^3}{3n_c^2 \theta + x^2}$ $a = \frac{(3x^2 + 1)[3n_c^3(\theta+h) + n_c x^2 + x^3] - 4x^5}{(3x^2 + 1)(3n_c^2 \theta + x^2)}$	$K = n_c \left(\frac{H+1}{H-1} \right)^{1/H}$ $s = n_c \frac{16H}{(H^2 - 1)[(H^2 - 1)\theta + 4]}$ $a = n_c \frac{(H-1)[(H+1)^2(\theta+h) + 4]}{(H+1)[(H^2 - 1)\theta + 4]}$

TABLE I: Expressions relating criticality parameters n_c , θ , and h to biochemical parameters a , s , and K (and H in the Hill model).

- Grzes, A. B. Murillo, P. T. Hawkins, L. R. Stephens, A. I. Lamond, and D. A. Cantrell, *Nature immunology* (2015).
[46] N. Friedman, L. Cai, and X. S. Xie, *Physical Review Letters* **97**, 168302 (2006).
[47] A. Mugler, A. M. Walczak, and C. H. Wiggins, *Physical Review E* **80**, 041921 (2009).
[48] J. W. Cotari, G. Voisinne, O. E. Dar, V. Karabacak, and

- G. Altan-Bonnet, *Science Signaling* **6**, ra17 (2013).
[49] J. L. Cardy and R. Sugar, *Journal of Physics A: Mathematical and General* **13**, L423 (1980).
[50] N. G. Van Kampen, *Stochastic processes in physics and chemistry*, vol. 1 (Elsevier, 1992).

Supplementary Information

CRITICAL VS. BIOCHEMICAL PARAMETERS

The criticality parameters n_c , θ , and h are given by Eq. 6 in the main text. For convenience, Table I gives the values of n_c and the expansion coefficients f_{n_c} , f'_{n_c} , and f'''_{n_c} , on which θ and h depend, in terms of the biochemical parameters of the Schlögl and Hill models. Table I also gives the algebraic inverse: expressions for the biochemical parameters a , s , and K in terms of the criticality parameters. In the Hill model H is an additional free parameter.

EXPERIMENTAL METHODS

The experimental data, along with a detailed description of the experimental methods, have been published previously in Ref. [21] of the main text. For the sake of completeness, in this section we briefly summarize the experimental system and methods.

Drug	Inhibits	Dose range (nM)	Shape of data point
PD325901	MEK	0.09–1000	Up-pointing triangle
AZD6244	MEK	2.4–5000	Down-pointing triangle
Trametinib	MEK	0.5–1000	Right-pointing triangle
Dasatinib	SRC	0.09–1000	Circle
Bosutinib	SRC	0.5–1000	Square
PP2	SRC	24–50,000	Diamond

TABLE II: Drugs and dose ranges used in the experiments. Doses are spaced logarithmically. Shapes are used for the data points in Figs. 3(c), 7, and 8.

The data investigate the inhibition of a complex signaling cascade, the antigen-driven MAP kinase activation in primary CD8+ mouse T cells. A natural way to stimulate T cells is to load a peptide, that is, a fragment of an antigenic protein (which the T cells are programmed to recognize), onto antigen-presenting cells. We achieve this by incubating RMA-S cells with antigen at 37 °C. At the same time, we harvest the spleen and lymph nodes of a RAG2^{-/-} OT1 mouse which has T cells specific only to the ovalbumin peptide with the amino acid sequence SIINFEKL. When we mix the OT1 T cells with the antigen-loaded RMA-S cells, we expose the OT1 T cells to their activating peptide. In response, the T cells activate their receptors through a SRC Family kinase (Lck). This triggers an enzymatic cascade through Ras-Raf-MEK-ERK leading to double phosphorylation of ERK, rendering it capable of communicating with the nucleus. The distribution of the abundance of doubly phosphorylated ERK (ppERK), a key factor in cell regulation, is the readout in Fig. 3 of the main text.

To measure the abundance of ppERK, we use fluorescence cytometry. Specifically, we introduce ppERK-targeted antibodies that are pre-conjugated with a fluorescent dye. Because antibodies are very effective at selectively attaching to their target molecule with negligible false-positives, the fluorescence intensity of the dye is proportional to the abundance of ppERK. To measure the intensity, approximately 30,000 cells per sample are passed one-by-one through a microfluidic device where they encounter a series of excitation lasers. Each cell yields one intensity value, and the histogram provides an estimate of the distribution of ppERK abundance across the population. We assume that the distribution across the population is a fair representation of the steady-state distribution of ppERK abundance of a single cell. This is reasonable (and is the accepted practice) since while the cells are alive and the experiment is taking place, they are in a dilute suspension (approximately 30,000 cells in 100 μ L), not close enough together to influence each other.

Cells are treated with various doses of inhibitory drugs. The drugs and dose ranges used in the experiments are given in Table II. In Figs. 3(c) of the main text, 7, and 8, the size of the data point is proportional to the log of the dose, and the shape of the data point indicates the drug, as listed in Table II.

Ref. [21] describes a biologically-driven analysis of the data by fitting to a Gaussian mixture model, together with more experiments which correlate the inhibition to a functional read-out days after the stimulus. Ref. [21] also proposes a biologically-motivated coarse-grained model that relies on detailed knowledge of the MAP-kinase cascade. Here we employ an orthogonal approach: we focus on understanding the universal features, making as few assumptions as possible, and requiring no prior knowledge of the biology.

EXPERIMENTAL DATA ANALYSIS

Due to the long-tailed nature of the experimental molecule number distributions, it is more numerically stable to analyze them in log space. Here we provide the necessary conversions between functions of the molecule number from our theory, and functions of the log intensity from the experiments. In this section, prime denotes a derivative of a function with respect to its argument (n for f ; ℓ for q , Q , and ϕ).

Variables

The intensity is proportional to molecule number, $I = I_1 n$, where I_1 is the intensity of one molecule. We record and analyze the log intensity $\ell = \log I$. Therefore we have

$$\ell = \log(I_1 n), \quad n = \frac{e^\ell}{I_1}. \quad (9)$$

Probability distributions

The molecule number distribution is p_n . Denote the distribution of ℓ as $q(\ell)$. Approximating n as continuous, probability conservation requires $p_n dn = q(\ell) d\ell$. Therefore

$$q(\ell) = \frac{p_n}{d\ell/dn} = np_n. \quad (10)$$

Feedback function

The feedback function is related to the probability distribution according to $f_n = np_n/p_{n-1}$ as in the main text. Using Eq. 10, the feedback function is written

$$f_n = \frac{np_n}{p_{n-1}} = (n-1) \frac{np_n}{(n-1)p_{n-1}} = (n-1) \frac{q(\ell)}{q(\tilde{\ell})}, \quad (11)$$

where, using Eq. 9,

$$\tilde{\ell} = \log[I_1(n-1)] = \log(I_1 n) + \log(1-\epsilon) \approx \ell - \epsilon. \quad (12)$$

The last steps define $\epsilon \equiv 1/n$ and assume that for most values of n with appreciable probability we have $\epsilon \ll 1$. Therefore Eq. 11 becomes

$$\begin{aligned} f_n &= n(1-\epsilon) \frac{q(\ell)}{q(\ell-\epsilon)} \approx n(1-\epsilon) \frac{q(\ell)}{q(\ell) - \epsilon q'(\ell)} = \frac{n(1-\epsilon)}{1 - \epsilon q'/q} \approx n(1-\epsilon) \left(1 + \epsilon \frac{q'}{q}\right) \approx n \left[1 + \epsilon \left(\frac{q'}{q} - 1\right)\right] \\ &= n + \frac{q'}{q} - 1, \end{aligned} \quad (13)$$

where we have kept only to first order in ϵ . Defining $\phi(\ell) \equiv f_n - n$, from Eq. 13 we have

$$\phi(\ell) = f_n - n = \frac{q'}{q} - 1 = Q'. \quad (14)$$

In the last step we define

$$Q(\ell) \equiv -\ell + \log q \quad (15)$$

so that ϕ is computed as a total derivative, which we find more numerically stable.

Maxima

Maxima are defined by $p'_{n_*} = 0$. Eq. 9 implies

$$\partial_n = I_1 e^{-\ell} \partial_\ell \quad (16)$$

Therefore, using Eqs. 9 and 10, the maxima condition reads

$$0 = \partial_n p = (I_1 e^{-\ell} \partial_\ell) \left(\frac{q}{n}\right) = I_1 e^{-\ell} \partial_\ell (I_1 e^{-\ell} q) = I_1^2 e^{-2\ell} (-e^{-\ell} q + e^{-\ell} q') = (I_1 e^{-\ell})^2 (q' - q). \quad (17)$$

We define points ℓ_* by

$$q'(\ell_*) = q(\ell_*). \quad (18)$$

Equivalently, by Eq. 14, the ℓ_* satisfy

$$\phi(\ell_*) = 0, \quad (19)$$

which is consistent with the interpretation of ϕ as the forcing. The maxima are obtained via Eq. 9:

$$n_* = \frac{e^{\ell_*}}{I_1}. \quad (20)$$

Critical point

The critical point n_c is defined by $f''_{n_c} = 0$. Using Eq. 16, this condition reads

$$0 = \partial_n^2 f = \partial_n^2(\phi + n) = \partial_n^2 \phi = (I_1 e^{-\ell} \partial_\ell)^2 \phi = I_1 e^{-\ell} \partial_\ell (I_1 e^{-\ell} \partial_\ell \phi) = I_1^2 e^{-\ell} (-e^{-\ell} \phi' + e^{-\ell} \phi'') = (I_1^2 e^{-\ell})^2 (\phi'' - \phi'). \quad (21)$$

We define a point ℓ_c by

$$\phi''(\ell_c) = \phi'(\ell_c), \quad (22)$$

and the critical point n_c is obtained via Eq. 9:

$$n_c = \frac{e^{\ell_c}}{I_1}. \quad (23)$$

Numerically we enforce Eq. 22 by writing it as $0 = \partial_\ell(\phi' - \phi)$, and therefore

$$\ell_c = \operatorname{argmax}_\ell (\phi' - \phi). \quad (24)$$

Derivatives

Derivatives of f with respect to n at n_c are related in a straightforward way to derivatives of ϕ with respect to ℓ at ℓ_c . First, the zeroth derivative is, by Eq. 14,

$$f_{n_c} = \phi(\ell_c) + n_c, \quad (25)$$

where n_c is given by Eq. 23. Then, using Eq. 16, the first derivative is

$$f'_{n_c} = \partial_n[\phi + n]_{n_c} = \partial_n[\phi]_{n_c} + 1 = [(I_1 e^{-\ell} \partial_\ell)\phi]_{\ell_c} + 1 = I_1 e^{-\ell_c} \phi'(\ell_c) + 1 = \frac{\phi'(\ell_c)}{n_c} + 1. \quad (26)$$

Finally, by a similar procedure, the third derivative is

$$f'''_{n_c} = \frac{1}{n_c^3} [\phi'''(\ell_c) - 3\phi''(\ell_c) + 2\phi'(\ell_c)] = \frac{1}{n_c^3} [\phi'''(\ell_c) - \phi'(\ell_c)], \quad (27)$$

where the second step uses Eq. 22.

Criticality parameters

Using Eqs. 23, 25-27, and 20, the criticality parameters defined in Eq. 6 of the main text are

$$m = \frac{n_* - n_c}{n_c} = e^{\ell_* - \ell_c} - 1, \quad (28)$$

$$\theta = \frac{2(1 - f'_{n_c})}{-f'''_{n_c} n_c^2} = \frac{-2\phi'(\ell_c)}{\phi'(\ell_c) - \phi'''(\ell_c)}, \quad (29)$$

$$h = \frac{2(f_{n_c} - n_c)}{-f'''_{n_c} n_c^3} = \frac{2\phi(\ell_c)}{\phi'(\ell_c) - \phi'''(\ell_c)}. \quad (30)$$

Note that they do not depend on I_1 .

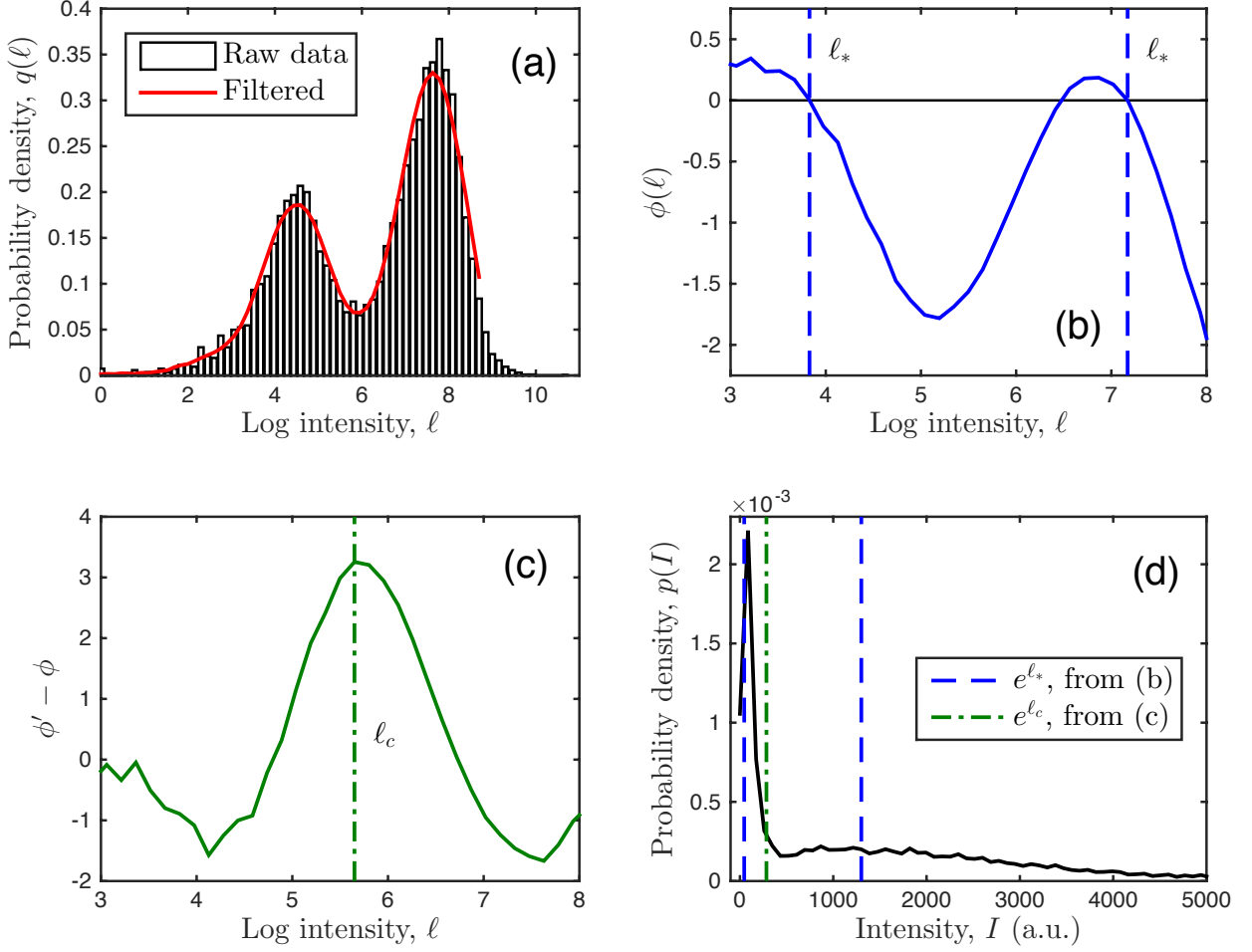


FIG. 4: Demonstration of analysis procedure for 3.4 nM of MEK inhibitor PD325901. (a) The distribution $q(\ell)$ of log intensity ℓ is plotted using $L = 100$ bins and Savitsky–Golay filtered using a window of $W = 25$ data points. (b, c) From the filtered data, we compute $\phi(\ell)$ to find ℓ_* , and $\phi' - \phi$ to find ℓ_c , as described in the text. (d) ℓ_* and ℓ_c give the maxima and critical point of the intensity distribution.

Savitsky–Golay filtering

To estimate derivatives, we apply Savitsky–Golay filtering to $q(\ell)$. Savitsky–Golay filtering replaces each data point with the value of a polynomial of order J that is fit to the data within a window W of the point. Since we require three derivatives of $\phi(\ell)$ (Eqs. 29 and 30), which depends on the first derivative of $q(\ell)$ (Eq. 14), we use the minimum value $J = 4$.

Analysis procedure

The analysis is demonstrated for an example experimental condition in Fig. 4. In summary, we:

1. plot $q(\ell)$ from the data using L bins [Fig. 4(a), black];
2. filter $q(\ell)$ using window W [Fig. 4(a), red];
3. compute ℓ_* using Eq. 19 [Fig. 4(b)];
4. compute ℓ_c using Eq. 24 [Fig. 4(c)];

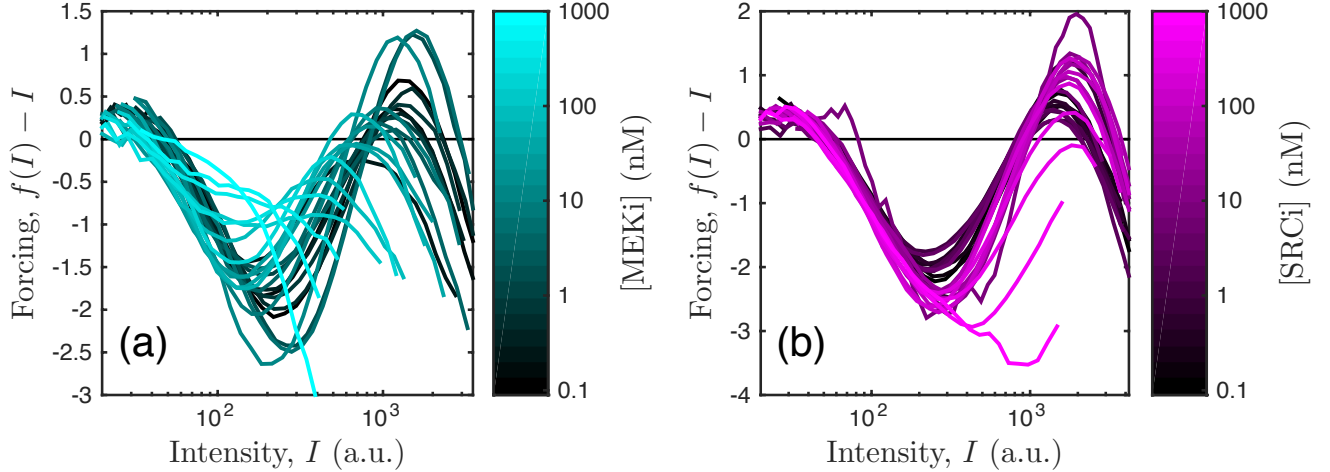


FIG. 5: Forcing function [equivalent to $\phi(\ell)$] at various doses of (a) MEK inhibitor PD325901 and (b) SRC inhibitor Dasatinib. We see that MEK inhibition drives the high-intensity stable fixed point to lower molecule numbers, whereas SRC inhibition does not, as expected from previous work (Ref. [21] of the main text).

5. compute m , θ , and h from ℓ_c , ℓ_* , and ϕ and its derivatives using Eqs. 28-30;
6. compute p_n from the data using I_1 ; and
7. compute C/k_B from p_n , θ , n_c (Eq. 23), f'''_{n_c} (Eq. 27), and f_n (Eq. 13) using Eq. 8 of the main text.

Fig. 4(d) shows the values of ℓ_* and ℓ_c overtop the intensity distribution $p(I)$. We see that the maxima fall where expected, and the critical point falls between the maxima as expected.

VALIDATION OF ANALYSIS

We validate the analysis in several ways, as described in the main text. One way is to investigate the effects of MEK and SRC inhibition on the high-molecule-number state. As described in Ref. [21] of the main text, previous work demonstrated that MEK inhibition drives the high state to lower molecule numbers, whereas SRC inhibition does not. Fig. 5 shows the results of our analysis for MEK inhibitor PD325901 [Fig. 5(a)] and SRC inhibitor Dasatinib [Fig. 5(b)]. We see that MEK inhibition drives the high-intensity stable fixed point to lower molecule numbers, whereas SRC inhibition does not, in agreement with the previous work.

FURTHER TESTS OF SCALING PREDICTIONS

The experimental data in Fig. 3(c) of the main text are plotted on a linear scale because they span a large range of m and θ values, and the linear scale allows one to test for features unique to the biochemical feedback model, such as the steep rise of the upper branch ($m > 0$) of the m vs. θ curve. It is also desirable to plot the data on a log-log scale, because doing so potentially allows one to compare with the scaling prediction shown in Fig. 2(a) of the main text, namely that $\beta = 1/2$. Two concerns arise when testing this prediction: (1) the presence of autofluorescence, which is known to affect the low-molecule number peak (see the section ‘Autofluorescence’ below), may make the scaling of the lower branch ($m < 0$) untrustworthy; and (2) a strict scaling test not only requires sufficient data near the critical point, but also requires that the unvaried parameter remain fixed (here, $h = 0$) — unfortunately, the original experiments were not designed with these considerations in mind.

Nonetheless, Fig. 6(a) shows the data of Fig. 3(c) on a log-log scale, and, despite these concerns, the results are very positive. First of all, we see that the data from the lower branch (red) are indeed not necessarily consistent with a slope of $\beta = 1/2$, potentially due to autofluorescence (concern 1 above), and therefore we focus on the upper branch (blue data). Due to concern 2 above, we focus on the data that are closest to $h = 0$ by making both the size and

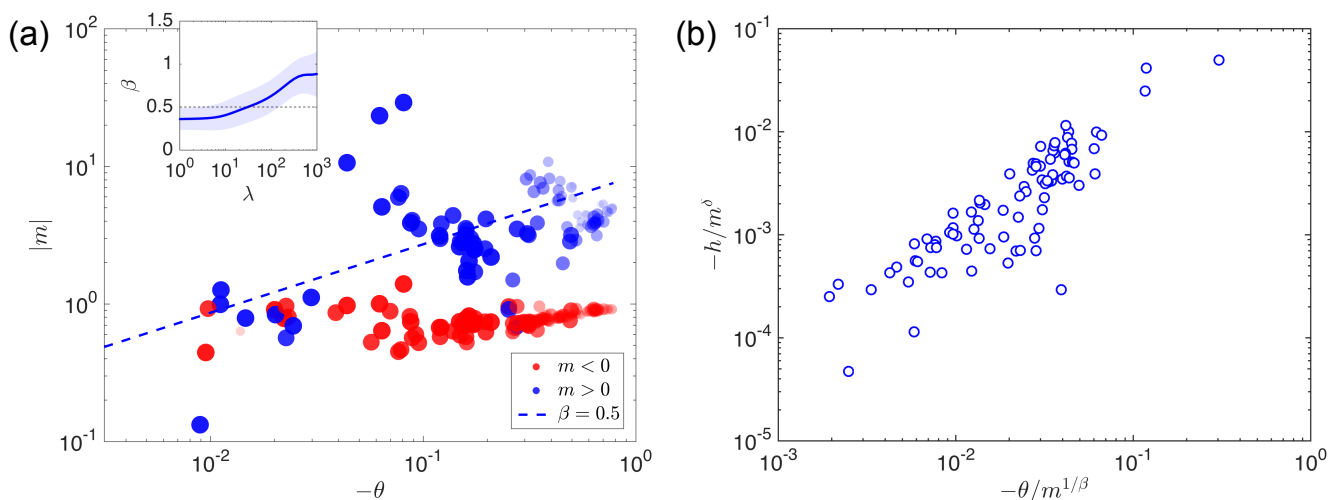


FIG. 6: Data from Fig. 3(c) of the main text are consistent with scaling predictions of the theory. (a) Data from Fig. 3(c) plotted on a log-log scale, with size and opacity inversely proportional to $|h|$. Whereas the lower-branch ($m < 0$) data (red) are potentially affected by autofluorescence (see text) and not necessarily consistent with the predicted slope $\beta = 1/2$, the upper-branch data (blue) are consistent with $\beta = 1/2$: the blue dashed line shows a guide to the eye, and the inset shows the slope and 95% confidence interval of a linear fit with weighting $e^{-\lambda|h|}$. We see from the inset that the slope ranges from approximately $\beta = 0.35$ at small λ to $\beta = 0.85$ at large λ , and contains $\beta = 1/2$ within its confidence interval for most of the range of λ . (b) Blue data from panel (a) plotted in terms of rescaled variables h/m^δ and $\theta/m^{1/\beta}$, using the predicted values $\beta = 1/2$ and $\delta = 3$. We see a rough collapse to a single function over several orders of magnitude.

opacity of the data points scale inversely with $|h|$ [equivalent to the use of color in Fig. 3(c)]. We see that the blue data are consistent with a slope of $\beta = 1/2$, as shown by the blue dashed line that is a guide to the eye. In fact, we see in the inset that when we perform a linear fit to the blue data with weighting strength $e^{-\lambda|h|}$, we find that the slope ranges from $\beta = 0.36$ at small λ to $\beta = 0.88$ at large λ , and contains $\beta = 1/2$ within its confidence interval for most of the range of λ . This not only shows consistency of the data with the prediction $\beta = 1/2$, but also largely excludes some plausible alternatives, such as $\beta = 1$. This makes us optimistic that future experiments that are specifically designed to probe this scaling may more accurately confirm (or disprove) the prediction $\beta = 1/2$.

To further address concern 2 above that h is not fixed at 0, we seek a scaling prediction that is compatible with the fact that none of m , θ , or h remains strictly fixed at its critical value within the experimental dataset. In fact, as described in Ref. [43] of the main text, a prediction of exactly this type exists for the Ising universality class: a plot of the rescaled variables h/m^δ vs. $\theta/m^{1/\beta}$ should collapse to a single function. In Fig. 6(b), we produce this plot for the blue data in Fig. 6(a), using the predicted values of $\beta = 1/2$ and $\delta = 3$. We see that the data do indeed roughly collapse to a single function, over several orders of magnitude. Together with Fig. 3(c) of the main text (including the inset, where the minimum provides strong evidence for $\alpha = 0$), Fig. 6 demonstrates consistency of the experimental data with the scaling exponents of the Ising universality class in the mean-field limit.

ROBUSTNESS OF RESULTS

Typically when working with distributions, the number of bins is an adjustable parameter. However, since here we also filter the distribution, changing the filter window is similar to changing the number of bins. That is, choosing a large number of bins L , but also a large window size $W < L$, is similar to choosing a small L . Therefore, we choose L to be sufficiently large to resolve the main features of the distribution, then focus on the adjustable parameter W/L . We find that $L = 100$ suffices (although we check L as low as 50 in what follows).

In principle, the parameter W/L varies from 0 to 1. $W/L = 0$ corresponds to no filtering, whereas $W/L = 1$ corresponds to using every data point in the filter, i.e., extreme over-filtering. In the main text we use $W/L = 25/100 = 0.25$ (Fig. 3). Here we investigate the robustness of the results to the value of W/L , focusing in particular on the behavior of the order parameter in Fig. 3(c) of the main text. As shown in Fig. 7, we vary W/L over the range 0.15 to 0.5 in two ways: we either vary W [Fig. 7(a)-(b)] or we vary L [Fig. 7(c)-(d)]. We see in Fig. 7 that in both

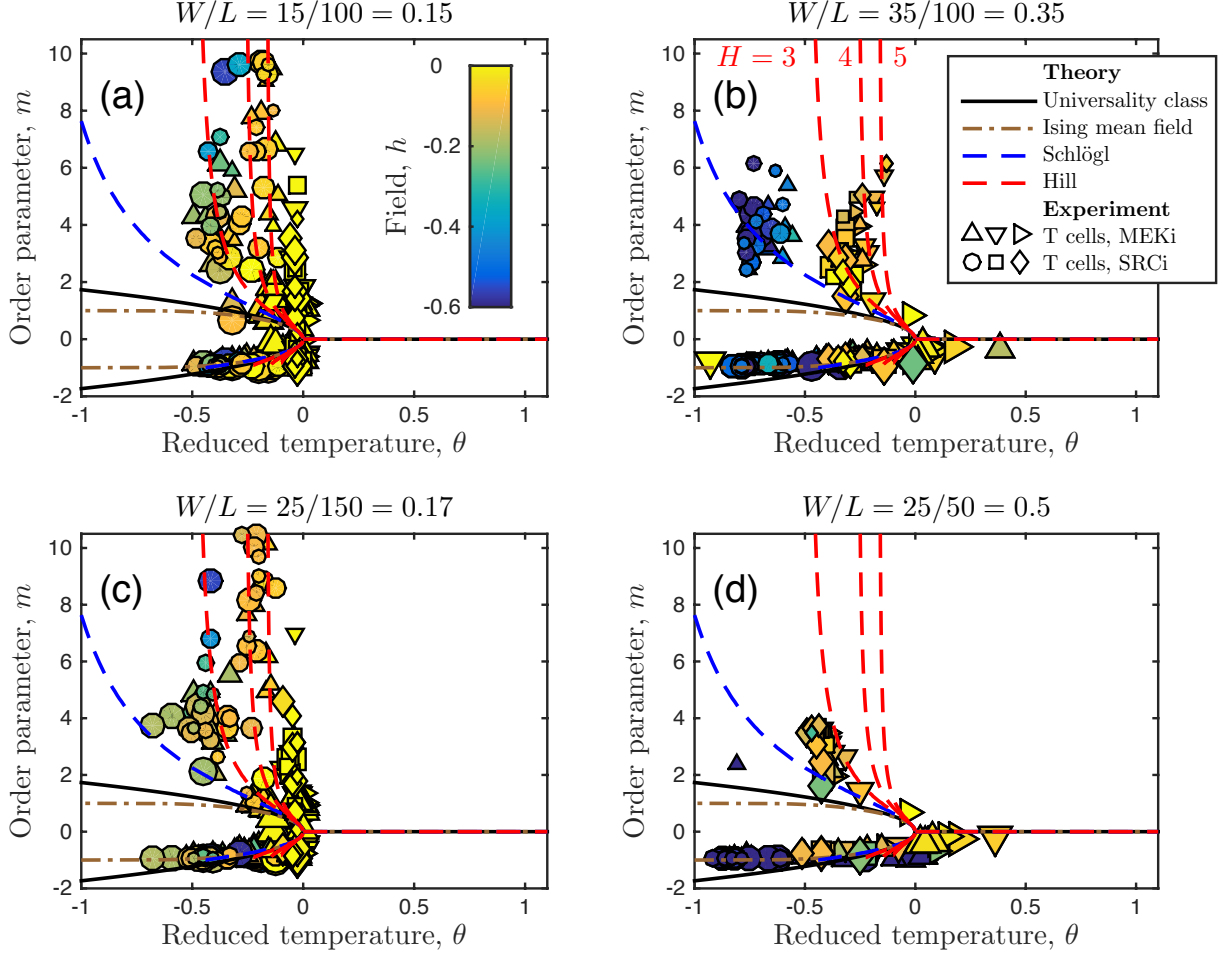


FIG. 7: Main features are robust to choice of W/L , as described in the text. Title of each panel indicates choices of W and L . See Table II for drugs (shape) and doses (size). Colorbar, legend, and H values in (a) and (b) apply to all panels. All theory curves take $h = 0$.

cases, the theory and the experimental data continue to agree in the same important ways noted in the main text: (i) no data exist between the branches; (ii) data near $m = \theta = 0$ have $h \approx 0$ (yellow); (iii) the data closely follow the lower branch and obey $m \geq -1$; and (iv) the data exhibit the steep rise of the upper branches in the biochemical models.

AUTOFLUORESCENCE

All cells, without any attached fluorescent antibodies, emit a wide range of frequencies at low intensity in response to the exciting lasers, called autofluorescence. The presence of autofluorescence means that the low-intensity readings in most flow cytometry experiments include contributions due inherently to the measurement technique. Here, it is possible that this effect increases the size of the low-intensity peak beyond the actual fluorescence intensity of ppERK. A larger low-intensity peak and a long tail are features that are consistent with negative values of the external field h , since negative h corresponds to biasing the peak of the distribution toward lower molecule numbers. Thus, autofluorescence may contribute to the fact that the data exhibit $h \lesssim 0$, as seen in Fig. 3(c) of the main text.

ABSOLUTE MOLECULE NUMBER

Absolute molecule number is set by the parameter I_1 . The heat capacity C provides a way to calibrate I_1 . Fig. 8 shows C for the theory and the experimental data using four values of I_1 over four orders of magnitude. In all cases, we see that both the theory and the data exhibit a global minimum at $\theta = h = 0$, which is a key prediction of the universality class ($\alpha = 0$). However, for $I_1 = 10$ [Fig. 8(a)] and $I_1 = 1$ [Fig. 8(b)] the minimum of the theory is higher than that of the data, while for $I_1 = 0.01$ [Fig. 8(d)] the minimum of the theory is lower than that of the data. Only for $I_1 = 0.1$ [Fig. 8(c); also Fig. 3(c) inset of main text] are the minima the same depth. We conclude that $I_1 = 0.1$ is the correct value, which corresponds, for example, to a value of $\bar{n}_c = 7,300$ molecules averaged across all experiments, and a value of $\bar{n}_* = 35,000$ molecules in the high mode averaged across all cases with no inhibitor.

The value of 35,000 ppERK molecules is consistent with previous measurements on these cells described in Refs. [44] and [45] of the main text. In these references it was estimated that there are approximately 100,000 and 150,000–250,000 ERK molecules per cell, respectively, and since only about 20–30% of these molecules are doubly phosphorylated during T cell receptor activation, we arrive at the estimate of roughly 30,000–50,000 ppERK molecules per cell. Thus, the heat capacity allows us to calibrate I_1 unambiguously and allows estimation of absolute molecule number from fluorescence data with strikingly plausible results.

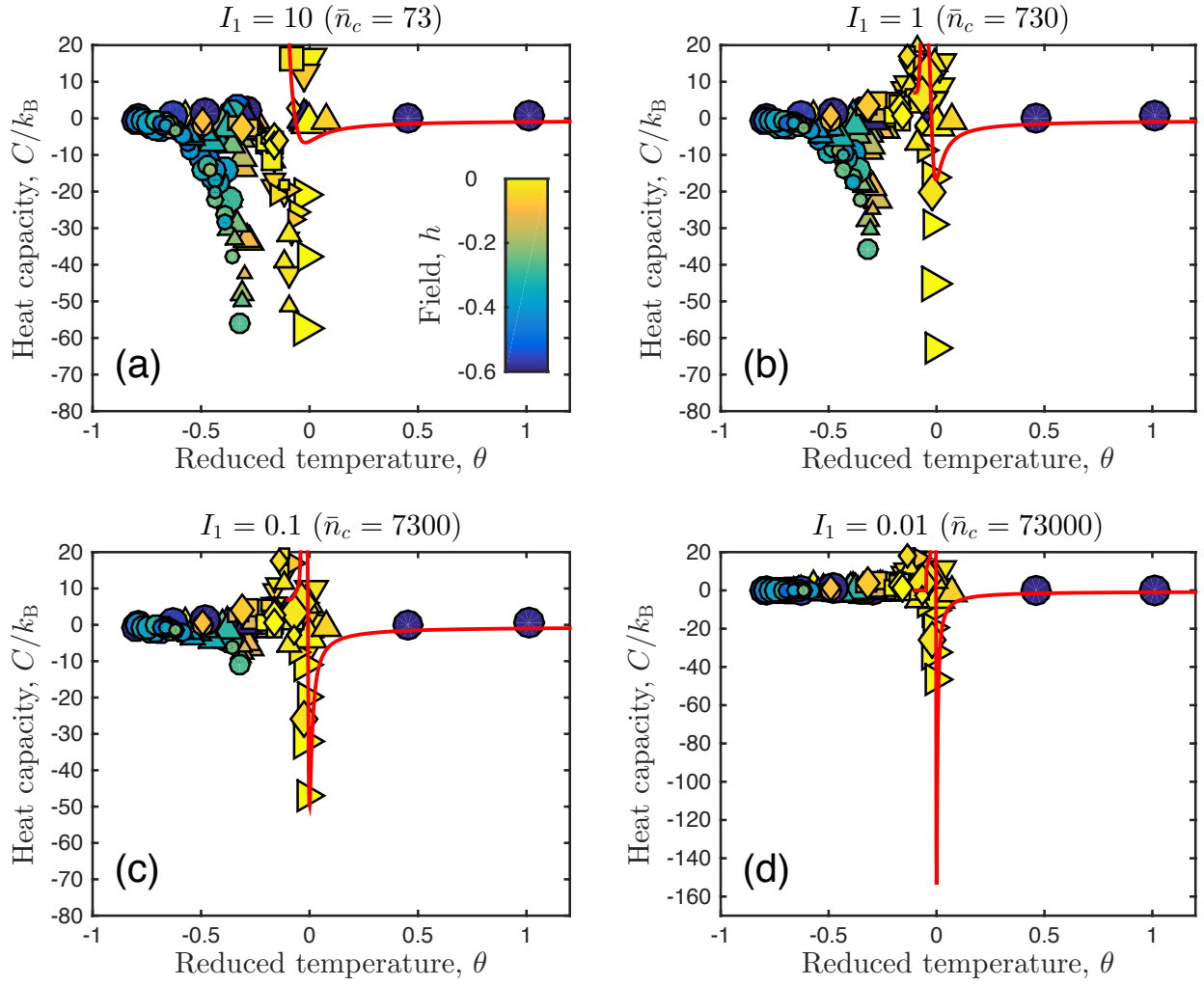


FIG. 8: Comparison of heat capacity theory with experimental data allows determination of I_1 , and therefore absolute molecule number. Titles of each panel indicate values of I_1 , and the corresponding value of \bar{n}_c averaged across all experiments. Only in (c) are the depths of the global minima in the theory and data the same. See Table II for drugs (shape) and doses (size). Colorbar in (a) applies to all panels. Theory curves are for Hill model with $h = 0$ and $H = 4$.